Thin Solid Films 540 (2013) 212–220

Contents lists available at SciVerse ScienceDirect

Thin Solid Films

journal homepage: www.elsevier.com/locate/tsf

Sensing devices based on ZnO hexagonal tube-like nanostructures grown on p-GaN heterojunction by wet thermal evaporation

H.I. Abdulgafour [a,b,*], Z. Hassan [a], F.K. Yam [a], C.W. Chin [a]

[a] Nano-Optoelectronics Research Laboratory, School of Physics, Universiti Sains Malaysia, 11800-Penang, Malaysia
[b] Ministry of Science and Technology, Baghdad, Iraq

ARTICLE INFO

Article history:
Received 4 July 2012
Received in revised form 13 May 2013
Accepted 17 May 2013
Available online 26 May 2013

Keywords:
ZnO nanostructures
Characterization
p–n heterojunction
Gas sensor
UV detector

ABSTRACT

High-quality ZnO hexagonal tube-like nanostructures grown on p-type GaN heterojunction have been synthesized for sensing applications through a low-cost catalyst-free process by thermal evaporation at 800 °C. The morphological, structural, and optical properties of the ZnO heterostructures have been examined. In this study, Pd/ZnO/Pd metal–semiconductor–metal gas sensor has been fabricated based on the ZnO tube-like nanostructures. The sensitivity of ZnO/p-GaN heterostructures is measured at different flow rates (25, 50, 100, and 150 sccm) of H_2 gas at room temperature. The highest response of the ZnO/p-GaN sensor was 1250%, when 150 sccm of H_2 gas was injected. In addition, Pd/Al n-ZnO/p-GaN heterojunction as an ultraviolet photodiode is demonstrated. The current–voltage curve of the heterojunction demonstrates obvious rectifying behavior in the dark and under illumination. For illumination conditions, one light source of wavelength 365 nm and another at 400 nm were used, sweeping the bias voltage from +4 to −4 V. Under UV light at 365 nm the current was almost 12 times greater than that in the dark, while under UV light at 400 nm the current was 2.2 times greater than that in the dark at 3 V.

1. Introduction

In recent years, low-dimensional systems have attracted tremendous interest in nanosensor applications due to their gas sensitivity, ultraviolet (UV) photoresponse, and optical transparency in the visible region, among other features [1–14]. In particular, quasi-one-dimensional nanowires or nanorods are a promising low-cost material for high-speed UV photoconductive nanoscale detectors and gas sensors [3,7–14].

In the past decade, research on wide band gap semiconductors has focused on zinc oxide (ZnO) due to its excellent properties as a semiconductor. Its high electron mobility, high thermal conductivity, good transparency, wide and direct band gap (3.37 eV), large exciton binding energy, and ease of fabrication into micro- and nanostructures make ZnO suitable for a wide range of applications in optoelectronics, transparent electronics, lasing, and sensing [15–18].

The fabrication of one-dimensional ZnO micro- and nanostructures has been demonstrated using various methods, including thermal evaporation, thermal chemical vapor deposition, metal organic chemical vapor deposition, and sol–gel process [19–21]. The thermal evaporation catalyst-free method is a simple and low-cost technique for growing metal oxide nanostructures. Several processing parameters such as temperature, pressure, carrier gas (including gas species and flow rate), type of substrate and evaporation duration can be controlled [22,23].

The growth of n-type ZnO on other p-type materials may provide an alternative way to realize ZnO-based p–n heterojunctions. Various heterojunctions of ZnO thin films have been achieved using p-type materials such as GaN, AlGaN, Si, CdTe, GaAs, and diamond [24–26]. The p-GaN materials are the best candidates for developing heterojunction-based light emitting diodes with n-ZnO because p-GaN has many advantages over other p-type materials. Both ZnO and GaN have the same wurtzite crystal structure, the same lattice parameters (lattice mismatch is only 1.8%), and almost the same band gaps 3.37 eV and 3.4 eV, respectively at room temperature [27–33].

The microstructural and physical properties of ZnO can be modified by introducing changes to the procedures of its chemical synthesis [34–39]. For example, ZnO nanotubes have been fabricated using a variety of approaches [41–43], such as optimization of the seed layer thickness [44], utilization of appropriate solvent compositions [45], ultrasonic pretreatment of the reaction solution [46], and post pH adjustment [47]. The ZnO nanotubes can be made by one-step growth methods or two-step growth and etching processes [45,48–50]. Nevertheless, it is accepted that the formation of ZnO nanotubes is a kinetically controlled process. The final morphology and dimension of the nanostructures are determined by competition between the adsorption and desorption of the precursor molecules, or, in other words, crystal growth and dissolution processes [51,52].

* Corresponding author at: Nano-Optoelectronics Research Laboratory, School of Physics, Universiti Sains Malaysia, 11800-Penang, Malaysia. Tel.: +60 174500286.
E-mail address: hind_alshaikh@yahoo.com (H.I. Abdulgafour).

0040-6090/$ – see front matter © 2013 Elsevier B.V. All rights reserved.
http://dx.doi.org/10.1016/j.tsf.2013.05.091

The controlled synthesis of nano- and micro-sized particles with different shapes and morphologies has attracted considerable interest, because the properties of nano- and microcrystals depend not only on their composition but also on their structure, phase, shape, size, and size distribution [53]. Besides activation of the crystallographic facets' exposure to target gases, a high surface-to-volume ratio is crucial, as mentioned above. However, a high surface-to-volume ratio can be obtained not only by reducing grain size, but also through a highly ordered pore structure, as in a mesoporous structure or nanotube arrays [54,55].

For gas sensing applications, ZnO is one of the promising metal oxide wide band gap semiconductors [33–35]. In gas sensing, ZnO has been tested for sensing harmful and toxic gases [36–38]. A common concern about gas sensors based on ZnO thin films is the lack of selectivity and higher operating temperature. In general, its optimum operating temperature is 400–450 °C [40]. Recently, Tien et al. [56] used Pt-coated ZnO nanorods as sensors that were capable of detecting part per million (ppm) concentrations of hydrogen at room temperature. Heo et al. [57] used Au islands for the site-selective growth of ZnO nanowires by molecular beam epitaxy (MBE) at 600 °C. Wang et al. [58,59] studied the response of Pd-coated ZnO nanorods to H_2 at ppm levels in N_2 and found them to be suitable for practical applications in hydrogen-selective sensing at room temperature. According to previous reports, the sensitivity of ZnO to gas may be affected by nanostructure surface defects and post-growth annealing in a H_2 or O_2 ambient [60–62].

In this study, an alternative method to synthesize high quality ZnO hexagonal tube-like nanostructures on p-GaN/Si by using wet thermal evaporation method without catalyst is presented. The simplicity, lower cost, and suitability of this method in producing high structural and optical quality ZnO nanostructures are very promising for efficient sensing applications; particularly the high surface area to volume ratio is the major factor responsible for high performance of the sensors fabricated based on ZnO hexagonal tube-like nanostructures. In this report, a device with 2-in-1 design has been demonstrated; this device consists on metal–semiconductor–metal (MSM) structure for gas sensing and p–n junction for UV detection.

In such device, the ZnO hexagonal tubes immediately below the metal contacts contribute to the sensing of the gas and UV diode devices, as the other ZnO nanorods are not directly connected to the contacts. In this work, a ZnO hexagonal tube-like nanostructure/p-GaN was developed to study the ability of these nanostructures for sensing applications.

2. Experimental details

2.1. Growth of p-GaN by molecular beam epitaxy

The epilayer was grown by Veeco GEN II plasma-assisted molecular beam epitaxy with standard elemental effusion cells consisting of group III materials, Mg dopant, and active nitrogen (produced by a Veeco Unibulk radio frequency plasma source). The nitrogen plasma was operated at 300 W. The Si (111) substrate was cleaned by the Radio Corporation of America method prior to load into the load lock chamber and being heated at 200 °C for 2 h. The substrate was subsequently transferred to the growth chamber and again heated at 900 °C for 20 min to remove surface contaminants.

The growth was carried out using high-purity material sources such as gallium (7N) and aluminum (6N5), while nitrogen with 7N purity was channeled to a radio frequency source to generate reactive nitrogen species. The growth of p-GaN was started by heating the substrate to 900 °C for outgassing. Then the substrate temperature was lowered to 850 °C for Ga cleaning before growth of the AlN buffer layer. Following the Ga cleaning step, an AlN buffer layer was grown at 850 °C for 30 min. Next, the substrate temperature was elevated to 800 °C to grow the GaN layer. The growth time was about 45 min. The final growth step took place at 840 °C. The film was p-doped by varying the Mg cell temperature from 360 °C to 380 °C. A p-type GaN layer with an AlN buffer was grown on an n-type Si (111) substrate of 3 in. The thickness of GaN film was about 0.6 μm [63].

2.2. Synthesis of ZnO heterostructures

Synthesis was carried out in a tube furnace (Thermolyne type F21100) with an inner diameter of 25 mm. Prior to the synthesis, a p-type GaN wafer substrate was cut into 1.2×1.2 cm^2 pieces and cleaned with acetone and isopropyl alcohol in an ultrasonic bath, followed by a rinse with distilled water; the wafers were then dried by nitrogen gas flow. A pure metallic Zn powder (99.9%) as the source material was placed into a ceramic boat. The p-GaN substrate was inserted into a quartz tube after the tube furnace has reached the desired temperature. For deposition in wet oxygen ambient, the gas was passed through a bath of water before being introduced into the furnace. The furnace was slowly heated from 400 °C to 800 °C. After reaching 800 °C, argon (Ar) and wet oxygen (O_2) gas were introduced with flow rates of 350 sccm and 126 sccm, respectively, for 1 h. After the evaporation, the alumina boat was slowly drawn out from the furnace and cooled to room temperature.

The ZnO hexagonal tube-like nanostructures were subsequently characterized by various tools. The surface morphology of the ZnO heterostructures was examined by scanning electron microscopy (SEM), model JOEL JSM-6460LV. For SEM characterization normally the measurements are performed at 10 kV to measure the surface morphology of the samples. A high-resolution X-ray diffractometer (HR-XRD) model PANalytical X'pert Pro MRD with a Cu-Kα_1 radiation source ($\lambda = 1.5406$ Å) is used to assess the crystalline quality as well as the phase identification. Under high resolution measurements, this system has a resolution of 12″. The XRD measurements are based on Bragg–Brentano configuration. The optical quality of the ZnO hexagonal tube-like nanostructures was studied at room temperatures by photoluminescence (PL) and Raman scattering. The measurements were performed by using Jobin Yvon HR800UV spectrometer system; a helium cadmium (He–Cd) laser (325 nm) and an argon ion laser (514.5 nm) were used as an excitation source for PL and Raman measurements, respectively. For both measurements, the incident laser power was 20 mW. A Keithley electrometer (Model 2400) was used to record the I–V characteristics for gas sensor and UV photodiode. All the experiments in the current work were performed under atmospheric pressure and at room temperature.

2.3. Fabrication of gas sensor

Fig. 1 shows the schematic diagram of the gas sensing system. To fabricate a p–n junction diode gas sensor, MSM with interdigitated contacts (electrodes) forming Schottky barriers was used, as shown in Fig. 2A. The Pd Schottky contact (150 nm thick) was deposited on a portion of ZnO/GaN sample using the A500 Edwards RF magnetron sputtering unit with a power sputtering of 150 W. The four fingers of each of the Pd contact electrodes were 0.23 mm wide and 4 mm long, with 0.4 mm spacing. The gas sensing experiments were carried out by using a homemade gas sensing chamber. For characterization of the gas sensing device, the test fixture was placed in the chamber with wires connected from the probes to Keithley device to measure the current voltage (I–V) characteristics of the sample. The voltage was biased from 1 V to −1 V and different flow rates of 2% H_2 in N_2 gas were used in this experiment.

2.4. Fabrication of the UV photodiode device

For the Schottky photodiode device, an Al contact (200 nm thick) was coated on the bottom of the Si (111) using a thermal evaporation system under a pressure of 2.55×10^{-7} Pa. To provide a Schottky

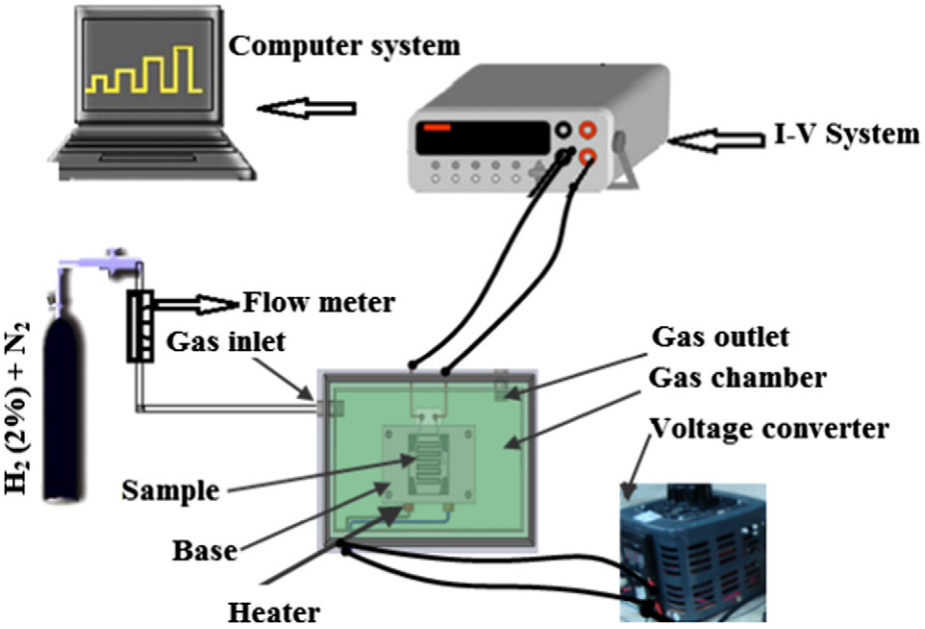

Fig. 1. Schematic diagram of homemade gas sensing system.

contact, Al and Pd electrodes were made on Si (111) and n-ZnO, respectively. Subsequently, the device was moved to the thermal furnace and annealed at 400 °C for 10 min, to form an effective Schottky contact. The schematic diagram of the device is shown in Fig. 2B. The (I–V) characteristic on the fabricated heterostructural p–n junction was carried out conventionally. In addition, the I–V characteristics of the UV diode were measured by sweeping the bias voltage from +4 V to −4 V both in dark and illuminated conditions at different UV diode sources. During photocurrent measurements, UV diodes of wavelengths 365 nm (UV 365) and 400 nm (UV 400) with a power density of 0.3 mW/cm^2 were used as an excitation source.

3. Results and discussions

3.1. Morphological analysis

Fig. 3A and B shows low- and high-magnification SEM images of the n-ZnO/p-GaN hexagonal tube-like nanostructures synthesized by wet thermal evaporation method at 800 °C. The average diameter of the ZnO nanostructures obtained on the p-type GaN substrate was approximately 600 nm for the hexagonal shape and the diameter of the tube hole was about 250 nm. Apart from that, Fig. 4A shows that the "blanket thickness" for as grown GaN substrate before deposited was 0.6 μm; also Fig. 4B shows that the "blanket thickness" for ZnO nanostructures grown on the p-type GaN substrate was around 1.5 μm, and the length of the tube was around 1 μm as shown in Fig. 4C.

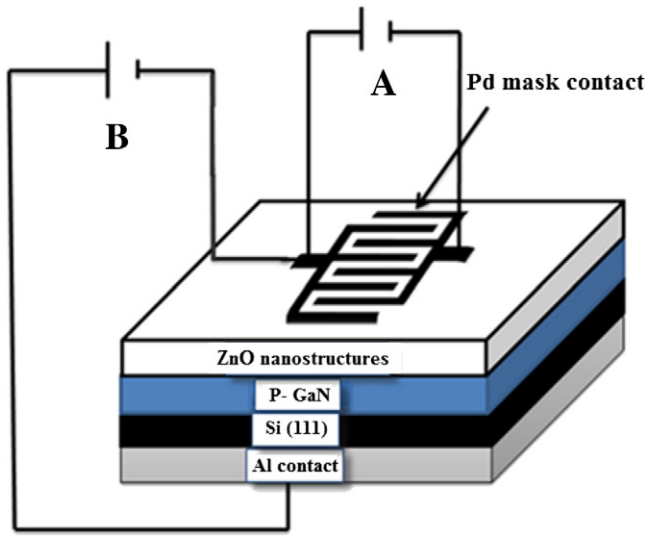

Fig. 2. The schematic diagram of ZnO/GaN p–n heterojunction was fabricated (A) for gas sensing device, and (B) for UV photodiode device.

3.2. XRD analysis

To further understand the influence of morphology differences on the properties of nanostructures, XRD was used to study the crystalline structure and alignment of products as well as to show the crystal size in the ZnO nanostructures. Fig. 5A shows the typical XRD pattern of n-ZnO hexagonal tube-like nanostructures grown on p-type GaN substrate, revealing the highly preferential *c*-axis orientation of ZnO heterostructures. Fig. 4B also shows that the ZnO nanostructures yield a sharp peak at 34.37°, which is attributable to the perfect *c*-axis of the ZnO (0 0 2) plane, while the sharp peak at 34.42° is attributable to the p-GaN (0 0 2) plane. An epitaxial relation exists between the GaN epitaxy film and the ZnO nanowires. Since GaN and ZnO have similar lattice constants, the c-axes in the XRD profiles of GaN and ZnO almost overlap [64].

The diffraction peaks in the pattern were indexed as hexagonal wurtzite ZnO nanostructures with lattice constants in accordance with the values in the standard card (JCPDS no. 36-1451 for ZnO). From the XRD pattern, *a* and *c* the lattice constants for ZnO were derived to be $a = 0.3252$ nm, and $c = 0.5098$ nm, consistent with the standard values for bulk ZnO. The XRD pattern reveals that the synthesized layer is polycrystalline. The peaks at 2θ values of 31.72°, 34.37°, 36.26°, 47.52°, and 62.82° correspond to the (1 0 0), (0 0 2), (1 0 1), (1 0 2), and (1 0 3) phases, respectively, of the hexagonal close-packed crystal structure of ZnO according to JCPDS.

The diffraction peak of the sample was indexed to that of the high-crystallinity hexagonal wurtzite ZnO. The ZnO hexagonal tube-like nanostructures yielded a sharp peak at 34.37°, attributable to the ZnO (0 0 2) plane. The (0 0 2) peak at 34.37° was the strongest peak, indicating that the ZnO sample was oriented dominantly along

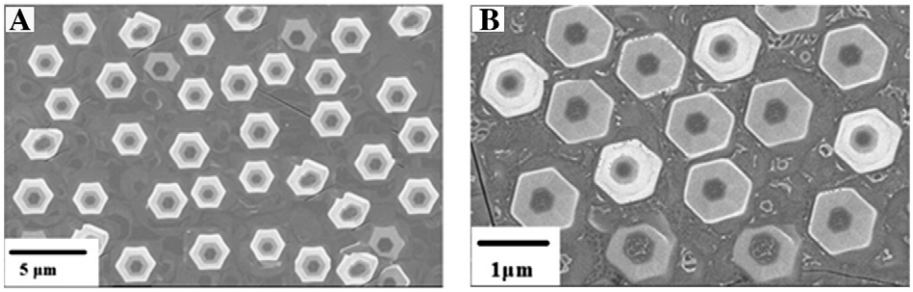

Fig. 3. (A, B) Low- and high-magnification SEM images of the ZnO hexagonal tube-like nanostructures synthesized by vapor solid mechanism at 800 °C.

the (0 0 1) growth direction, while the peaks at (1 0 0), (1 0 1), (1 0 2), and (1 1 0) indicated that nonepitaxial growth occurred.

Fig. 5 also shows that the intensity of the (0 0 2)-oriented peak (*c*-axis orientation) was higher in the ZnO nanostructures on the GaN substrate, which can be attributed to the low surface free energies of the (0 0 2) plane. From literature [65–67], (0 0 2) is the highest-density plane with the lowest free energy. Furthermore, the strong intensity and narrow width of the ZnO diffraction peaks also indicated that the resulting products had high crystallinity.

3.3. Optical analysis

3.3.1. PL analysis

Fig. 6 shows the room-temperature PL spectrum of n-type ZnO hexagonal tube-like nanostructures grown on p-GaN separately. From Fig. 6, the spectrum shows two dominant peaks: one in the near-UV region (340–400 nm) and one in the visible region (400–620 nm). The UV luminescence reveals the crystal quality and visible luminescence displays structural defects [71]. The ZnO nanostructures exhibited a strong UV emission corresponds to the near band-edge (NBE) emission. This NBE is attributed to the recombination of band-edge free excitons through an exciton–exciton collision process [68,69] (at room temperature) caused by NBE electron transition [70]. The green band in the visible luminescence, known as deep-level emission, was attributed to the radiative recombination of the photogenerated hole with the electrons that belong to singly ionized oxygen vacancies [72,73]. Therefore, the peak at 500 nm is due to the photogenerated hole in the valance band, with an electron occupying the deep oxygen vacancy energy band.

The peak position of the UV emission was found to be 372 nm for ZnO hexagonal tube-like nanostructures grown on p-GaN, as shown in Fig. 6. The band edge UV emission is typically observed at 362 nm for the p-GaN substrate. From literature bulk ZnO is well-known to exhibit a UV emission of ~380 nm, nevertheless the ZnO nanostructures in this work was found to be blue-shift significantly to 372 nm. Thus, the blue shift in the UV emission was possible because the tensile strain became more intense as the diameter of the ZnO nanostructure increased [74]. The higher blue shift luminescence observed in comparison with the energy gap of bulk ZnO is due to its surface state. A broadening of the band gap energy occurs with the decrease in crystallite size. Our results show that a higher blue shift luminescence is attributed to charge carrier quantum confinement.

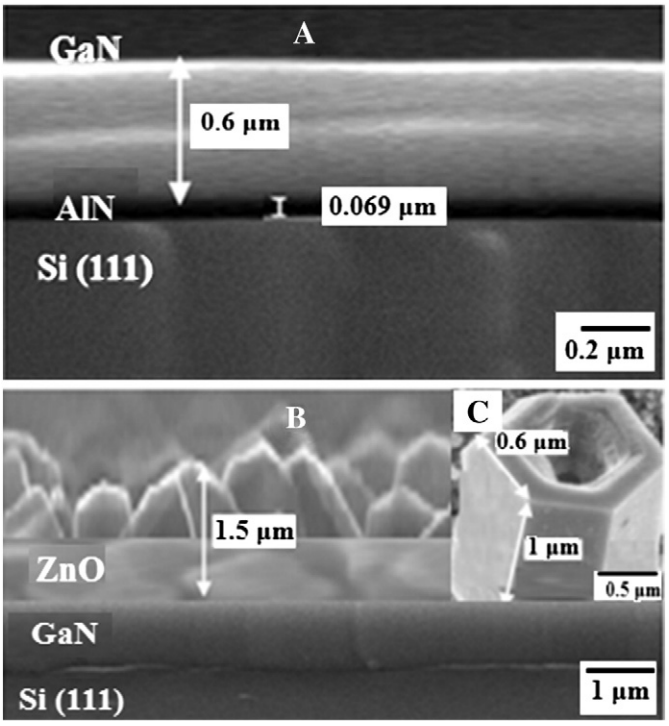

Fig. 4. SEM cross-section images (A) for p-GaN substrate before deposited, and (B) for ZnO hexagonal tube-like nanostructures grown on a p-GaN substrate.

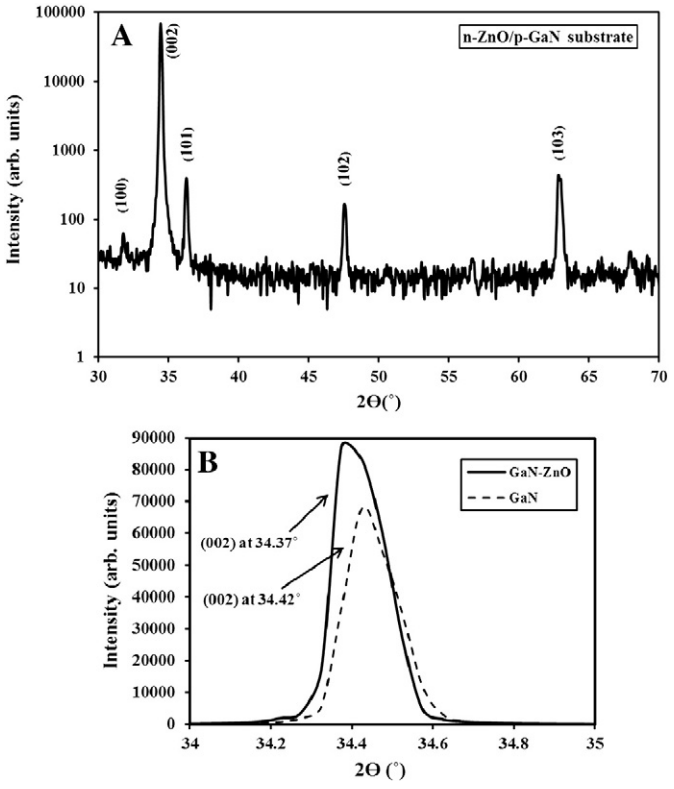

Fig. 5. (A) The XRD pattern of ZnO hexagonal tube-like nanostructures grown p-GaN substrate at 800 °C, and (B) the shift peak of (002) plane and the X-ray diffraction patterns of both p-GaN film and n-type ZnO nanostructures.

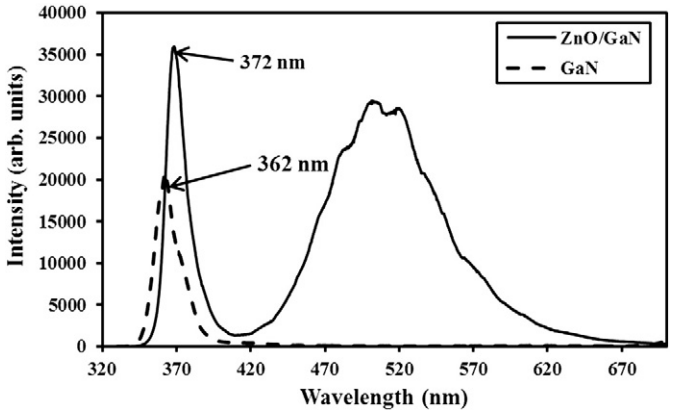

Fig. 6. Room temperature photoluminescence spectrum for ZnO hexagonal tube-like nanostructures grown on p-GaN substrate at 800 °C.

This indicates that the particles are formed in a lower dimension and the probability of the recombination of the electrons and holes is higher in low-dimensional structures. This state leads to high emission efficiency from the substrates due to quantum confinement effects. Reducing the dimensions to nanometres drastically changes the physical properties of the ZnO structure.

3.3.2. Raman scattering analysis

Fig. 7 shows the Raman scattering spectrum observed at room temperature of the ZnO hexagonal tube-like nanostructures grown on p-GaN substrate at 800 °C. Raman scattering is sensitive to the crystal quality, structural defects, and disorders of the grown products. The ZnO wurtzite-type hexagonal structure belongs to the C_{6V}^4 space group with two formula units per primitive cell and there are eight sets of optical phonon modes at the Γ point of the Brillouin zone, classified as $A_1 + 2B_1 + E_1 + 2E_2$ modes (Raman active), $2B_1$ modes (Raman silent), and $A_1 + E_1$ modes (infrared active). The E_1 mode is a polar mode and is split into transverse optical (TO) and longitudinal optical (LO) branches [75].

The Raman spectrum was excited by a 488-nm laser line. The peak at 519 cm^{-1} is attributed to the contribution from the oxidized Si substrate. The peaks at 326 cm^{-1}, 373 cm^{-1}, 437 cm^{-1}, and 568 cm^{-1} are assigned to E_2H–E_2L, A_1T, E_2H, and A_1L of the bulk ZnO, respectively. As shown from the spectrum, a sharp, strong, and dominant E_2 (high) mode of ZnO nanostructures located at 438 cm^{-1} is observed, which is the intrinsic characteristic of the Raman-active mode of wurtzite hexagonal ZnO [76]. This result is also consistent with the XRD analysis. Two very small peaks at 326 cm^{-1} and 373 cm^{-1} were assigned to the E_2H–E_2L (multi-phonon process) and A_1T modes, respectively. The peak at 568 cm^{-1} in the spectrum was also assigned to the E_2H mode for the GaN substrate.

In a comparison of the main E_2H peak with theoretical values, it is worth noting that E_2H is blue shifted in ZnO hexagonal tube-like nanostructures and the peak shift is $+2$ cm^{-1} [77,78]. The blue shift in E_2 (high) can be due to optical phonon confinement by nanostructures, laser induced heating, and/or phonon localization through defects or impurities in the nanostructures or due to anisotropic internal strains corresponding to different growth directions. The presence of the high intensity E_2 mode with the suppressed and very weak E_1L peak in Raman scattering indicates that the synthesized ZnO hexagonal tube-like nanostructures have good crystal quality and possess a wurtzite hexagonal crystal structure.

3.4. I–V characterization for hydrogen gas sensors

Fig. 8 shows the I–V characteristics of the Pd/ZnO hydrogen gas sensors operating with H_2 gas at flow rates of 25 sccm, 50 sccm, 75 sccm, 100 sccm, 125 sccm, and 150 sccm at room temperature. The sensor was found to show good Schottky behavior and a remarkable increase in current at different flow rates of H_2 gas for the ZnO hexagonal tube-like nanostructures grown on GaN substrate was observed at room temperature.

The series resistance evaluated from I–V curves for the Pd/ZnO/GaN Schottky diode measured at 300 K with different flow rates is shown in Fig. 9. The series resistance decreased exponentially upon introduction of a different flow rate of 2% H_2 in N_2 gas for the ZnO hexagonal tube-like nanostructures grown on a p-GaN substrate. Assuming that thermionic emission is the predominant mechanism, from I–V characteristics, the Schottky barrier heights for the two samples for different flow rates of hydrogen can be calculated based on the following two equations [79]:

$$I_d = I_0 \exp\left(\frac{qV_d}{nkT}\right)\left[1 - \exp\left(\frac{-qV_d}{kT}\right)\right] \quad (1)$$

where V_d is the voltage across the diode, n is the ideality factor, k is the Boltzmann constant, and I_0 is the saturation current given by

$$I_0 = AA^{**}T^2 \exp\left[\frac{-q\varphi_B}{kT}\right] \quad (2)$$

where q is the electron charge, T is the temperature, A is the contact area, A^{**} is the effective Richardson constant, and φ_B is the Schottky barrier

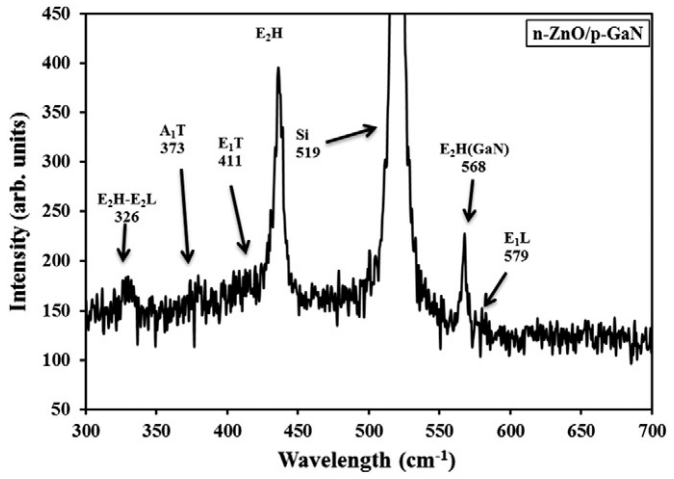

Fig. 7. Raman spectrum for ZnO hexagonal tube-like nanostructures grown on p-GaN substrate.

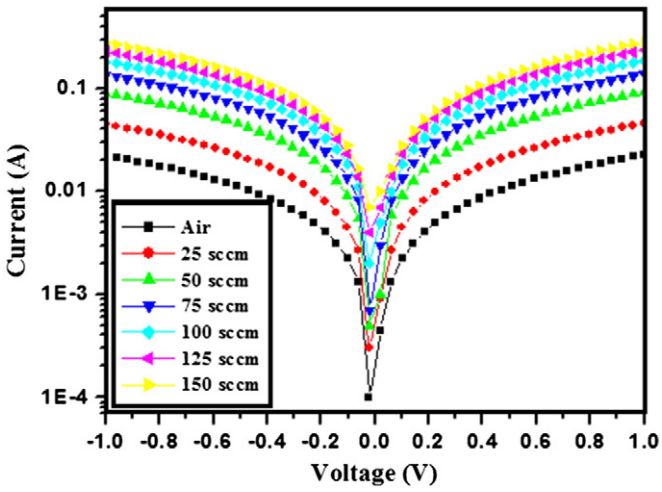

Fig. 8. The (I–V) characteristics at room temperature of Pt/ZnO hexagonal tube-like nanostructures grown on p-GaN as a function to hydrogen flow rate.

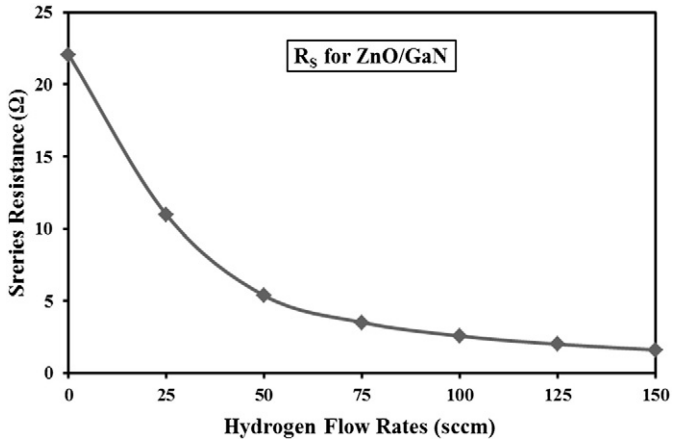

Fig. 9. The series resistance at room temperature of Pd/ZnO hexagonal tube-like nanostructures grown on p-GaN substrate as a function of hydrogen flow rate.

height. The theoretical value of A^{**} is (32 A cm^{-2} K^{-2}) based on the effective mass ($m^* = 0.27m_e$) of n-ZnO and ($A^{**} = 4\pi q m^* k^2 / h^3$). The values of the barrier heights of the nanostructure of the ZnO hexagonal tubes at different hydrogen flow rates are shown in Fig. 10.

The barrier height could be seen to have decreased gradually with the hydrogen flow rate in the Pd/ZnO sensor. The decrease in the barrier height is therefore due to a change in the (ϕ_{Pd}) Pd work function ($\varphi_B = \phi_{Pd} - \chi_s$). This decrease in barrier height with flow rate justifies the increase in current and the decrease in series resistance. This means that the ZnO hexagonal tube-like nanostructure surface coated with Pd provides a larger surface area, which allows hydrogen molecules to dissociate and form atomic hydrogen more efficiently.

For an ideal Schottky diode, the ideality factor (n) should be near unity, but in a real situation, it may increase when the effects of series resistance and leakage current become significant. The ideality factor for the Schottky diode is observed to increase with flow rate, as shown in Fig. 11.

Sensitivity is an important sensor characteristic. It is defined as [29]

$$S = \frac{I_{H_2} - I_{Air}}{I_{Air}} \quad (3)$$

where I_{H_2} and I_{Air} are the current in a H_2 containing ambient and in an air ambient, respectively. Fig. 12 shows the variation in sensitivity with the H_2 flow rate at room temperature for the sensor at 1 V. One can observe that the sensitivity increases linearly with the hydrogen flow rate for the sensor and Pd/ZnO is more sensitive to hydrogen, especially at the high hydrogen flow rate of 150 sccm; the sensitivity was 1250% at room temperature.

The dynamic response of the sensor based on ZnO hexagonal tube-like nanostructures for different H_2 flow rates at room temperature is shown in Fig. 13A. This figure shows the consecutive current responses of devices with time when the H_2 flow rates were reduced sequentially, from 150 sccm to 100 sccm to 50 sccm. The sensor response is defined as the variation in operating current due to interaction with the target gas. The adsorption and desorption times for H_2 were set at 10 min (H_2 on) and 15 min (H_2 off), respectively.

The response time is defined as the time taken for the sensor to reach 90% of the current from the initial value, while the recovery time is defined as the time taken from the current to reach 10% of its value after exposure of the test gas with the surface of the sensor. Fig. 13B shows the repeatability and on–off responses of the sensor measured at room temperature, with a constant voltage of 1 V. The response and recovery times measured for the sensor were about 4.5 and 6 min, respectively. Fig. 14 shows the analysis/plot of the rise time and recovery time as a function of H_2 gas concentrations.

The sensing mechanism is based on the reactions that occur at the sensor surface, between the surface of the ZnO nanostructure and the H_2 molecules to be detected. It is well known that oxygen molecules in air adsorb onto the surface of the ZnO layer to form O^{-2}, O^-, and O^{-2} ions, depending on the temperature, by extracting electrons from the conduction band [80]. The positively charged surface state and negatively charged adsorbed oxygen ions form a depletion region at the surface. A reducing gas such as H_2 gets oxidized to H_2O, consuming chemisorbed oxygen from the sensor surface by releasing electrons into the conduction band. This mechanism results in a reduction of the surface depletion region to increase the film conductivity that corresponds to the gas concentration.

Compared with conventional ZnO thin films, the observed enhancement in the gas sensing properties of the ZnO hexagonal tube-like nanostructure gas sensor is most likely attributable to the relatively higher degree of surface reaction due to the high specific surface area associated with the nanostructure. Based on our simple calculation, ZnO nanostructure sample has 2.48 times higher specific surface area than the ZnO without nanostructures. On the other hand, a comparison of ZnO hexagonal tube-like nanostructures with other nanostructures leads us to conclude that the gas sensing properties also depend on other factors, including crystallinity and surface properties, and these need to be studied further.

3.5. I–V characteristics for a p–n heterojunction photodiode device

Fig. 15 shows the I–V characteristics of the fabricated p–n heterojunction photodiode measured in the dark and under illumination

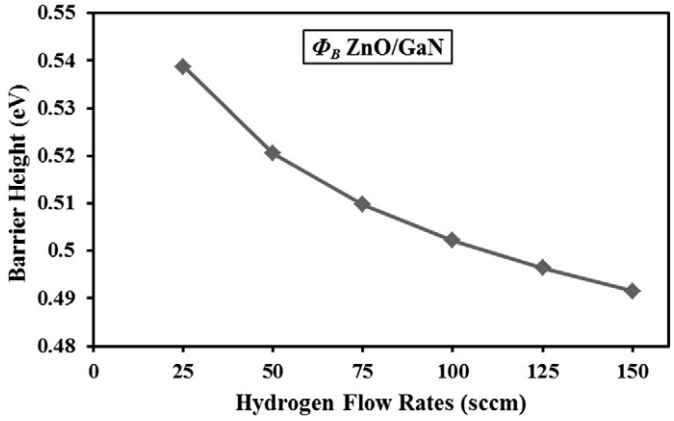

Fig. 10. The barrier height (φ_B) of Pd/ZnO gas sensors as a function of hydrogen flow rate at room temperature.

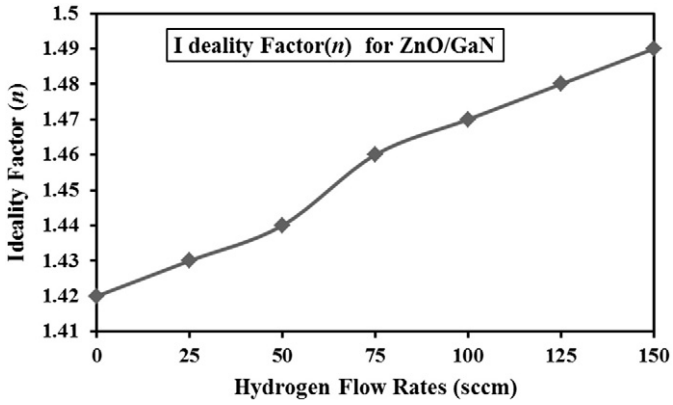

Fig. 11. The ideality factor (n) of Pd/ZnO gas sensors as a function of hydrogen flow rate.

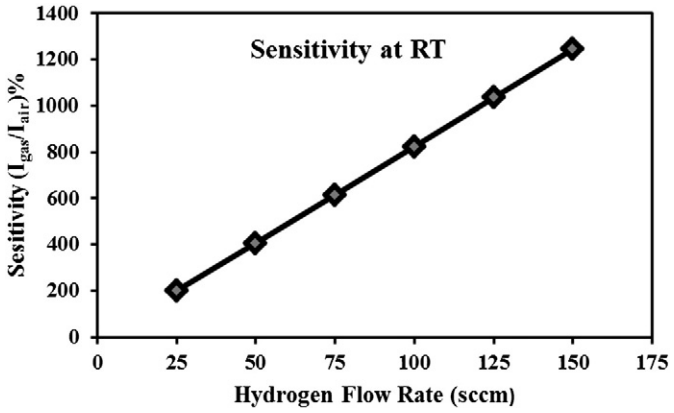

Fig. 12. The sensitivity of Pd/ZnO hexagonal tube-like nanostructures gas sensor at different flow rates.

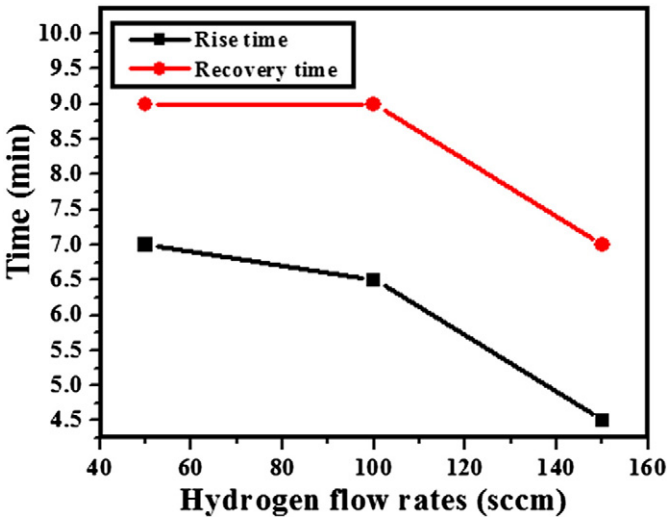

Fig. 14. The plot of rise time and recovery time with H_2 concentration.

with wavelengths of 365 nm and 400 nm. The I–V characteristics in the dark and under illumination were measured by changing the bias voltage from +4 V to −4 V (Fig. 15). From Fig. 15, typical rectifying behavior IF/IR is defined as the ratio of the forward current to the reverse current at the particular voltage. The values of the IF/IR with a high breakdown voltage that were obtained for dark, UV365, and UV400 lights are 17.9, 19.1, and 20.2, respectively, at 3 V (see Table 1). The turn-on voltage appeared at 0.7 V under forward bias with forward resistances in the dark and two UV lights obtained to be 1.66 kΩ, 0.77 kΩ, and 0.15 kΩ, respectively. Under reverse bias, the leakage currents at −1 V for the dark, UV400, and UV365 were observed at 7.6×10^{-5} A, 1.6×10^{-4} A, and 7.3×10^{-4} A, respectively. The leakage current is due to the imbalance between the carrier partial currents, which is caused by the difference in carrier concentration and mobility of the p and n layers [81]. The high current for the applied voltage (V_{ap}) is due to the low resistance of the metal semiconductor contacts. Hence, the V_{ap} between the palladium and aluminum contacts can be divided into two parts: the voltage drops at the contacts (V_c) and the voltage from the p–n junction (V_j) [82].

According to Fig. 2, which schematically depicts a fabricated p–n heterojunction photodiode device, Pd/Al was employed as the electrodes for ZnO and p-GaN. The theory of a p–n junction photodiode detector is different from that of an MSM-type photodetector. The operation of the detector in a photodiode involves three steps: (a) the generation of an electron–hole (e–h) pair by the absorption of incident light, where the photon energy exceeds the band gap of the material(s) in the device; (b) the separation and transportation of e–h pairs by the internal electric field; and (c) the interaction of the current with the external circuit to generate an output signal [83].

Hence, the I–V characteristic of a photodiode in the dark is similar to that of a normal rectifying diode. If the p–n junction is not formed, the generated e–h pair will form an ohmic character in the I–V curve and change the resistance. When the photodiode with a p–n junction is illuminated with optical radiation, the I–V characteristic should be

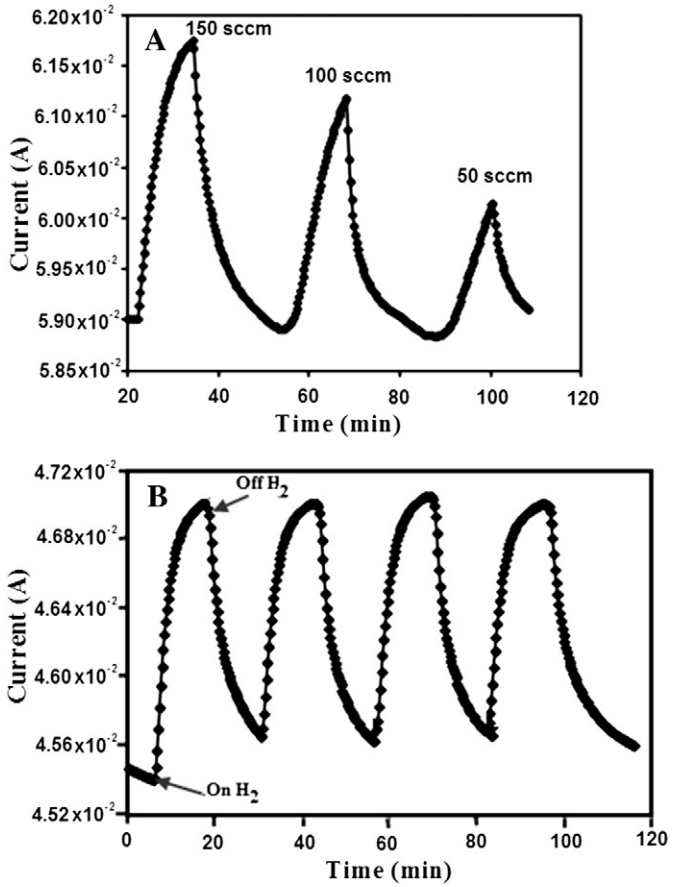

Fig. 13. (A) The on–off currents of ZnO gas sensors operating at room temperature for a constant voltage of 1 V exposed to different hydrogen flow rates. (B) Repeatability and the response current of the device with time when the H_2 flow rate is 150 sccm.

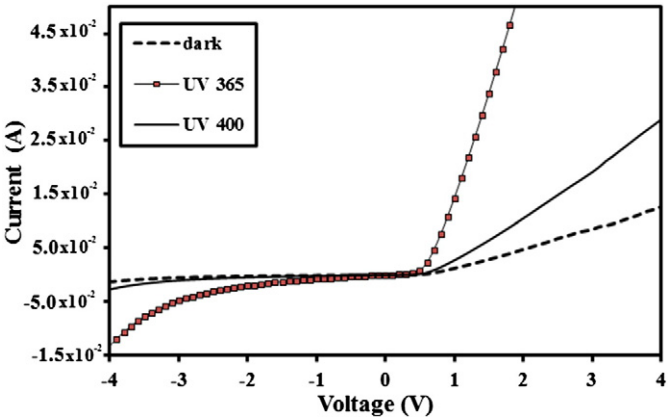

Fig. 15. The (I–V) characteristics of p–n heterojunction Pd/Al ZnO nano-hexagonal tubs photodiode measured in the dark and under illumination with wavelengths of 365 nm and 400 nm.

Table 1
The saturation current Is (nm), barrier height φ_B (eV), ideality factor (n), IF/IR at 3 V, resistance (R) kΩ at 0.7 V, and series resistance (Rs) Ω for p–n heterojunction Pd/ZnO/Al photodiode device.

Pd/ZnO/Al photodiode	Saturation current (Is) (A)	Barrier height φ_B (eV)	Ideality factor (n)	IF/IR at 3 V	Resistance R (kΩ) at 0.7 V	Series resistance Rs (Ω)	Leakage current at −1 V (A)
Dark	8.7×10^{-8}	0.7634	1.75	17.9	1.66	158	7.6×10^{-5}
UV (400 nm)	1.6×10^{-7}	0.7476	1.68	19.1	0.77	19	1.6×10^{-4}
UV (365 nm)	3.3×10^{-7}	0.7286	1.47	20.2	0.15	11.7	7.3×10^{-4}

shifted according to the photocurrent and reverse current. The measured current in photodiode I_m is given by

$$I_m = I_d + I_{ph} \tag{4}$$

where I_d is the dark current and I_{ph} is the photocurrent. By measuring the reverse current, we can ensure that our photoresponse is due to the p–n junction and not to ZnO nanostructures or p-GaN. In measurement under illumination, UV light passes through the ZnO hexagonal tube-like nanostructures and e–h pairs are produced in the ZnO nanostructures when the energy of the UV light (at 365 nm and 400 nm) is absorbed. The e–h pairs are separated by the internal electric field and the photocurrent is simultaneously generated.

4. Conclusions

In summary, two devices for H_2 gas sensors and p–n heterojunction photodiodes have been fabricated based on ZnO hexagonal tube-like nanostructures synthesized at 800 °C by a catalyst-free vapor solid technique through a simple, low-cost process on p-type GaN substrate under ambient conditions. The highest response of the ZnO/p-GaN gas sensor was 1250% when 150 sccm of H_2 gas was injected. This response is 3.5 times higher than that of ZnO nanorods grown by a sonochemical route. On the other hand, a fabricated p–n heterojunction photodiode measured in the dark and under illumination with wavelengths of 365 nm and 400 nm showed good rectifying behavior at 3 V with a high breakdown voltage. This study expects that the proposed process can also be readily utilized in the development of other one-dimensional semiconductor nanomaterial-based chemical and optoelectronic sensors.

Acknowledgment

The authors would like to acknowledge financial support by the ERGS Research Grant from the Universiti Sains Malaysia.

References

[1] Y.W. Heo, D.P. Norton, L.C. Tien, Y. Kwon, B.S. Kang, F. Ren, S.J. Pearton, J.R. LaRoche, Mater. Sci. Eng. R. 7 (2004) 1.
[2] Q.H. Li, Y.X. Liang, Q. Wan, T.H. Wang, Appl. Phys. Lett. 85 (2004) 6389.
[3] C. Soci, A. Zhang, B. Xiang, S.A. Dayeh, D.P.R. Aplin, J. Park, X.Y. Bao, Y.H. Lo, D. Wang, Nano Lett. 7 (2007) 1003.
[4] L. Chow, O. Lupan, H. Heinrich, G. Chai, Appl. Phys. Lett. 94 (2009) 163105.
[5] O. Lupan, L. Chow, G. Chai, A. Schulte, S. Park, H. Heinrich, Mater. Sci. Eng. B 157 (2009) 101.
[6] O. Lupan, L. Chow, G. Chai, H. Heinrich, S. Park, A. Schulte, J. Cryst. Growth 311 (2008) 152.
[7] O. Lupan, L. Chow, G. Chai, Microelectron. Eng. 85 (2008) 2220.
[8] O. Lupan, G. Chai, L. Chow, Microelectron. J. 38 (2007) 1211.
[9] G. Chai, O. Lupan, L. Chow, H. Heinrich, Sensors Actuators A Phys. 150 (2009) 184.
[10] O. Lupan, L. Chow, G. Chai, L. Chernyak, O. Lopatiuk-Tirpak, H. Heinrich, Phys. Status Solidi A 205 (2008) 2673.
[11] J. Suehiro, N. Nakagawa, S. Hidaka, M. Ueda, K. Imasaka, M. Higashihata, T. Okada, M. Hara, Nanotechnology 17 (2006) 2567.
[12] M. Law, D.J. Sirbuly, J.C. Johnson, J. Goldberger, R.J. Saykally, P. Yang, Science 305 (2004) 1269.
[13] Q.H. Li, Q. Wan, Y.X. Liang, T.H. Wang, Appl. Phys. Lett. 84 (2004) 4556.
[14] X.D. Bai, P.X. Gao, Z.L. Wang, E.G. Wang, Appl. Phys. Lett. 82 (2003) 4806.
[15] A. Janotti, C.G. Van de Walle, Rep. Prog. Phys. 72 (2009) 126501, (29 pp.).
[16] M. Willander, O. Nur, Q.X. Zhao, L.L. Yang, M. Lorenz, B.Q. Cao, J. Zúñiga Pérez, C. Czekalla, G. Zimmermann, M. Grundmann, A. Bakin, A. Behrends, M. Al-Suleiman, A. El-Shaer, A. Che Mofor, B. Postels, A. Waag, N. Boukos, A. Travlos, H.S. Kwack, J. Guinard, D. Le Si Dang, Nanotechnology 20 (2009) 332001.
[17] Z.L. Wang, Mater. Today 7 (2004) 26.
[18] Ü. Özgür, Ya.I. Alivov, C. Liu, A. Teke, M.A. Reshchikov, S. Doğan, V. Avrutin, J. Appl. Phys. 98 (2005) 1.
[19] M.H. Huang, S. Mao, H. Feick, H. Yan, Y. Wu, H. Kind, E. Weber, R. Russo, P. Yang, Science 292 (2001) 1897.
[20] S-W. Kim, S. Fujita, S. Fujita, Appl. Phys. Lett. 86 (2005) 153119.
[21] W.I. Park, G.-C. Yi, Adv. Mater. 16 (2004) 87.
[22] F. Krumeich, H.J. Muhr, M. Niederberger, F. Bieri, B. Schnyder, R. Nesper, J. Am. Chem. Soc. 121 (1999) 8324.
[23] J. Song, X. Wang, E. Riedo, Z.L. Wang, J. Phys. Chem. B 109 (2005) 9869.
[24] H.T. Ng, J. Li, M.K. Smith, P. Nguyen, A. Cassell, J. Han, M. Meyyappan, Science 300 (2003) 1249.
[25] S.B. Ogale, Thin Films and Heterostructures for Oxide Electronics, Springer, New York, 2005.
[26] N.H. Nickel, E. Terukov, Springer, 2005.
[27] U. Ozgur, Y.I. Alivov, C. Liu, A. Teke, M.A. Reshchikov, S. Dogan, V. Avrutin, S.J. Cho, H. Morkoc, J. Appl. Phys. 98 (2005) 041301.
[28] In: C. Jagadish, S.J. Pearton (Eds.), Zinic Oxide Bulk, Thin Films, and Nanostructures, Elsevier, New York, 2006.
[29] C.X. Wang, G.W. Yang, H.W.Y.H. Han, J.F. Luo, C.X. Gao, G.T. Zou, Appl. Phys. Lett. 84 (2004) 2427.
[30] X.D. Chen, C.C. Ling, S. Fung, C.D. Beling, Y.F. Mei, R.K.Y. Fu, G.G. Siu, P.K. Chu, Appl. Phys. Lett. 88 (2006) 132104.
[31] Y. Alivov, E.V. Kalinina, A.E. Cherenkov, D.C. Look, B.M. Ataev, A.K. Omaev, M.V. Chukichev, D.M. Bagnall, Appl. Phys. Lett. 83 (2003) 4719.
[32] J.A. Aranovich, D. Golmyo, A.L. Fahrebruch, R.H. Bube, J. Appl. Phys. 51 (1980) 4260.
[33] Q. Qin, L.W. Guo, Z. Zhou, H. Chen, X.I. Du, Z.X. Mel, J.F. Jia, Q.K. Xue, J.M. Zhou, Chin. Phys. Lett. 22 (2005) 2298.
[34] Y. Alivov, J.E.V. Nostrand, D.C. Look, B.M. Ataev, A.K. Omaev, Appl. Phys. Lett. 83 (2003) 2943.
[35] C.M. Ghimbeu, J. Schoonman, M. Lumbreras, M. Siadat, Appl. Surf. Sci. 253 (2007) 7483.
[36] R. Ferro, J.A. Rodriguez, P. Bertrand, Phys. Status Solidi C 2 (2005) 3754.
[37] H. Nanto, T. Minami, S. Takata, J. Appl. Phys. 60 (1986) 482.
[38] H. Morkoc, U. Ozgur, Zinc Oxide: Fundamentals, Materials and Device Technology, Wiley, 2009.
[39] M. Tiemann, Chem. Eur. J. 13 (2007) 8376.
[40] J.H. Lee, Sensors Actuators B 140 (2009) 319.
[41] L. Vayssieres, K. Keis, A. Hagfeldt, S.E. Lindquist, Chem. Mater. 13 (2001) 4395.
[42] J. Zhang, L.D. Sun, C.S. Liao, C.H. Yan, Chem. Commun. 3 (2002) 262.
[43] G.W. She, X.H. Zhang, W.S. Shi, X. Fan, J.C. Chang, Electrochem. Commun. 9 (2007) 2784.
[44] Y. Sun, G.M. Fuge, N.A. Fox, D.J. Riley, M.N.R. Ashfold, Adv. Mater. 17 (2005) 2477.
[45] H. Jiang, J. Hu, F. Gu, C.J. Li, Alloys Compd. 478 (2009) 550.
[46] Z. Wang, X.F. Qian, J. Yin, Z.K. Zhu, Langmuir 20 (2004) 3441.
[47] K. Yu, Z.G. Jin, X.X. Liu, J. Zhao, J.Y. Feng, Appl. Surf. Sci. 253 (2007) 4072.
[48] L.G. Yu, G.M. Zhang, S.Q. Li, Z.H. Xi, D.Z. Guo, J. Cryst. Growth 299 (2007) 184.
[49] Y. Xi, J.H. Song, S. Xu, R.S. Yang, Z.Y. Gao, C.G. Hu, J. Mater. Chem. 19 (2009) 9260.
[50] A.L. Yang, Z.L. Cui, Mater. Lett. 60 (2006) 2403.
[51] Y.H. Tong, Y.C. Liu, C.L. Shao, Y.X. Liu, C.S. Xu, J.Y. Zhang, Y.M. Lu, D.Z. Shen, X.W. Fan, J. Phys. Chem. B 110 (2006) 14714.
[52] S. Xu, Y. Shen, Y. Ding, Z.L. Wang, Adv. Funct. Mater. 20 (2010) 1493.
[53] B. Geng, C. Fang, F. Zhan, N. Yu, Small 4 (2008) 1337.
[54] G.S. Devi, T. Hyodo, Y. Shimizu, M. Egashira, Sensors Actuators B 87 (2002) 122.
[55] A. Cabot, J. Arbiol, A. Cornet, J.R. Morante, F. Chen, M. Liu, Thin Solid Films 436 (2003) 64.
[56] L.C. Tien, P.W. Sadik, D.P. Norton, L.F. Voss, S.J. Pearton, H.T. Wang, B.S. Kang, F. Ren, J. Jun, J. Lin, Appl. Phys. Lett. 87 (2005) 222106.
[57] Y.W. Heo, V. Varadarajan, M. Kaufman, K. Kim, D.P. Norton, F. Ren, P.H. Fleming, Appl. Phys. Lett. 81 (2002) 3046.
[58] H.T. Wang, B.S. Kang, F. Ren, L.C. Tien, P.W. Sadik, D.P. Norton, S.J. Pearton, J. Lin, Appl. Phys. Lett. 86 (2005) 243503.
[59] J.Y. Son, S.J. Lim, J.H. Cho, W.K. Seong, H. Kim, Appl. Phys. Lett. 93 (2008) 053109.
[60] Y.W. Heo, D.P. Norton, L.C. Tien, Y. Kwon, B.S. Kang, F. Ren, S.J. Pearton, J.R. LaRoche, Mater. Sci. Eng. R Rep. 47 (2004) 1.
[61] M.W. Ahn, K.S. Park, J.H. Heo, J.G. Park, D.W. Kim, K.J. Choi, J.H. Lee, S.H. Hong, Appl. Phys. Lett. 93 (2008) 263103.
[62] Y. Zhang, A. Kolmakov, S. Chretien, H. Metiu, M. Moskovits, Nano Lett. 4 (2004) 403.

[63] C.W. Chin, F.K. Yam, K.P. Beh, Z. Hassan, M.A. Ahmad, Y. Yusof, S.K. Mohd Bakhori, Thin Solid Films 520 (2011) 756.
[64] C.-H. Chen, S.-J. Chang, S.-P. Chang, M.-J. Li, I.-C. Chen, T.-J. Hsueh, C.-L. Hsu, Appl. Phys. Lett. 95 (2009) 223101.
[65] H.I. Abdulgafour, F.K. Yam, Z. Hassan, K. Al-Heuseen, M.J. Jawad, J. Alloys Compd. 509 (2011) 5627.
[66] N.H. Tran, A.J. Hartmann, R.N. Lamb, J. Phys. Chem. B 103 (1999) 4264.
[67] J. Lee, W. Gao, Z. Li, M. Hodgson, J. Metson, H. Gong, U. Pal, Appl. Phys. A 80 (2005) 1641.
[68] H. Deng, J.J. Russell, R.N. Lamb, B. Jiang, Thin Solid Films 458 (2004) 43.
[69] L. Vayssieres, Adv. Mater. 15 (5) (2003) 464.
[70] D.G. Zhao, S.J. Xu, M.H. Xie, S.Y. Tong, H. Yang, Appl. Phys. Lett. 83 (4) (2003) 677.
[71] S. Mridha, D. Basak, Phys. Status Solidi A 206 (2009) 1515.
[72] Y.W. Heo, D.P. Norton, S.J. Pearton, J. Appl. Phys. 98 (2005) 073502.
[73] H. Zeng, G. Duan, Y. Li, S. Yang, X. Xu, W. Cai, Adv. Funct. Mater. 20 (2010) 561.
[74] J.S. Lee, K. Park, M.I. Kang, I.W. Park, S.W. Kim, W.K. Cho, H.S. Han, S.S. Kim, J. Cryst. Growth 254 (2003) 423.
[75] C.X. Xu, X.W. Sun, Z.L. Dong, Y.P. Cui, B.P. Wang, Cryst. Growth Des. 7 (2007) 541.
[76] A. Khan, W.M. Jadwisienczak, H.J. Lozykowski, M.E. Kordesch, Physica E 39 (2007) 258.
[77] S. Choopun, N. Hongsith, P. Mangkorntong, N. Mangkorntong, Physica E 39 (2007) 53.
[78] A. Khan, J. Pak Mater. Soc. 4 (1) (2010) 5.
[79] Y.J. Xing, Z.H. Xi, Z.Q. Xue, X.D. Zhang, J.H. Song, R.M. Wang, J. Xu, Y. Song, S.L. Zhang, D.P. Yu, Appl. Phys. Lett. 83 (2003) 1689.
[80] V.L. Rideout, Solid State Electron. 18 (1975) 541.
[81] E. Oh, H.Y. Choi, S.H. Jung, S. Cho, J.C. Kim, K.H. Lee, S.W. Kang, J. Kim, J.Y. Yun, S.H. Jeong, Sens. Actuators B 141 (2009) 239.
[82] L. Balakrishnan, P. Premchander, T. Balasubramanian, N. Gopalakrishnan, Vacuum 85 (2011) 881.
[83] L. Lei, Z. Yanfeng, S.M. Samuel, L. Liwei, Sensors Actuators A Phys. 127 (2006) 201.